Tunable Dual-Band High-Impedance Coil for Wireless Power Transfer Applications

Ali Jabbari, Constantin Simovski, and Masoud Sharifian Mazraeh Mollaei

Abstract—Earlier, we engineered a wireless power transfer (WPT) system whose key element is a self-activating and self-decoupling transmitting (Tx) antenna called the high-impedance coil (HIC) that grants a high efficiency for a receiving (Rx) antenna with a free position in front of the Tx array. When the Rx antenna is located in front of the Tx one, the input impedance of the last one drastically decreases, which results in efficient power transfer. This impedance is initially so high that the Tx antenna in the absence of the Rx one does not accept power, which implies negligible open-circuit losses. This feature grants the automatic activation/deactivation of the WT system. In the present work, we suggest the qualitative modification of the HIC-based WPT system aiming its operation at two very different frequencies. The upper frequency is above 500 MHz which was earlier considered technically not achievable for HICs. To analytically engineer and describe our new HIC, in which the cable is replaced by a stripline, we developed a comprehensive semianalytical model. This model is quite general and can be used for further modifications of such antennas.

Index Terms—Circuit model, high-impedance coil (HIC), loop antenna, wireless power transfer (WPT).

I. Introduction

FOR decades, the realization of cheap, tunable, and highly efficient wireless power transfer (WPT) systems has been one of the main foci of research for radio engineers. Many efforts have been made to overcome various limitations on the performance of transmitting (Tx) and/or receiving (Rx) antennas. However, there are still difficulties in the realization of affordable and efficient WPT systems for several applications, for example, those where two (or more) operation frequency bands are required, where the displacement of the Rx is allowed, and high-power transfer efficiency needs to be maintained for moving receivers. In this article, we consider WPT devices based on antennas of the magnetic dipole type, which are most useful when the distance between the Tx and Rx antennas is not necessarily very small compared to the antenna size [1].

One known solution allowing displacements of an Rx device in a plane parallel to that of the Tx antenna(s) is to make a large Tx antenna so that its magnetic flux would cover all possible locations of the Rx [2], [3], [4], [5], [6]. Another solution is to make an array of Txs, so that the Tx in front of which the Rx is located would be active and the other Tx antennas would be inactive [7], [8], [9]. In the first case, the WPT system is cumbersome and not efficient because the Rx catches only a small part of the magnetic flux of the Tx coil. In the second case, tracking the Rx position is needed to activate and deactivate each of the Txs depending on the presence or absence of an Rx in front of them [1], [10], [11], [12], [13]. In a recent work, [14] one proposed a multiple-Tx WPT system without a control circuit. However, that self-activating technique was developed only for frequencies much lower than 100 MHz. Recently, a strong demand was claimed for WPT systems operating at frequencies above 100 MHz, and for multiband WPT systems [15]. In industrial applications, dual-band and multiband WPT systems are necessary due to higher reliability since different frequencies correspond to different channels. Moreover, dual-band WPT systems grant the opportunity of simultaneous power and data transfer [15]. Indeed, the use of higher frequencies (above 300–500 MHz) enables data transfer that is much faster than that possible at low frequencies utilized in conventional WPT systems. In some biomedical applications, simultaneous power and data transfer is a necessary requirement [16], [17]. In dual-band WPT systems dedicated to deep implants, each channel needs to be used either for power or for data transfer depending on the position of the implant [17]). These challenges make the conventional technical solutions for WPT not suitable. Researchers should find new ways.

A so-called high-impedance coil (HIC) based on split cable was suggested and studied in works [18], [19] for planar arrays of Rx antennas of magnetic dipole type dedicated for operation at a frequency lying between 70 and 300 MHz. The replacement of usual loop antennas by HICs allowed one to drastically reduce the parasitic mutual coupling in the Rx array. This is possible because the intrinsic input impedance of an Rx HIC is very high, whereas the mutual impedance between two coplanar HICs is modest. This property results in low coupling between the elements of the array. Together with a small electromagnetic size and simplicity of fabrication this property (in [18], it was called self-decoupling) made HICs promising for magnetic resonance imaging (MRI) systems [18], [19], [20], [21], [22]. In our work [20], an HIC was modified to ensure self-decoupling in both Tx and Rx regimes. Furthermore, we found that the HIC is advantageous for WPT

systems [23]. An HIC operating in the Tx regime is sensitive to the position of another magnetic dipole antenna in front of it. If there is no loop antenna in front of the Tx HIC, its input impedance is very high. Then the current in it as well as the dissipated and radiated powers are very low. This is the same as the deactivation of the Tx, although it is connected to the power source. When an Rx of nearly the same overall size is placed in front of this Tx (at a distance of the order of the loop diameter or smaller), a strong coupling between two antennas arises and results in the drop of the input impedance of the Tx antenna. Its current increases and the power efficiently transfers from the Tx to the Rx so that this power drastically exceeds P_{FS}—that radiated to free space by the WPT system [23]. It means that the Tx HIC is automatically activated or deactivated depending on the position of the Rx.

In [20], a new transceiver HIC for operating at 298 MHz was proposed and an array of eight such HICs was studied. We have shown good decoupling of these antennas in both Rx and Tx regimes. In [21], we introduced a dual-band HIC and showed the decoupling of the Tx and Rx arrays at both operating frequencies—121 and 298 MHz. However, HICs from [20] and [21] were radio-frequency coils for ultrahigh field MRI setups. As to the general concept of HICs for WPT systems with a freely positioned Rx, our work [23] left some issues unsolved. First, this HIC was made of a coaxial cable that is restrictive if the operating frequency should be essentially above 300 MHz. Simply scaling the design of [23] to high operation frequencies would result in a cable loop of so small diameter that it cannot be fabricated of a usual coaxial cable and special cables with an elastic/corrugated shield are expensive and their use would increase the cost of the antenna. Meanwhile, the HIC based on broken striplines which is suggested in the present work is not only cheap, but also advantageous because: 1) metal strips are printed on a printed circuit board (PCB) that disables the restrictions on the antenna geometry; 2) a stripline can be made with various characteristic impedance that allows us to engineer the desired frequency bands of operation; and 3) a multiband operation of the WPT systems can be easily engineered with it due to the easy physical access to all strips and degrees of freedom.

In this article, we suggest and study a dual-band stripline-based HIC that can be future generalized for more operation bands. We also study a WPT system comprising a coplanar array of such Tx antennas and an Rx antenna with variable positions. This work is not a marginal extension of [23]. The replacement of the cable with a symmetric stripline grants a qualitative change in the antenna properties. It allows us to engineer a dual-band WPT system with drastically different operation frequencies. For the first time (to our knowledge), one has achieved a highly efficient WPT in a system with variable positions of the Rx at frequencies so different as 540 and 131 MHz. Moreover, the previously known analytical model, efficient and accurate for cable-based HICs, turned out to be not capable of correctly describing the operation of our new HIC, especially at the upper frequency. Therefore, for this work, we developed a new circuit model of our new HIC and engineered the dual-band operation of the WPT system
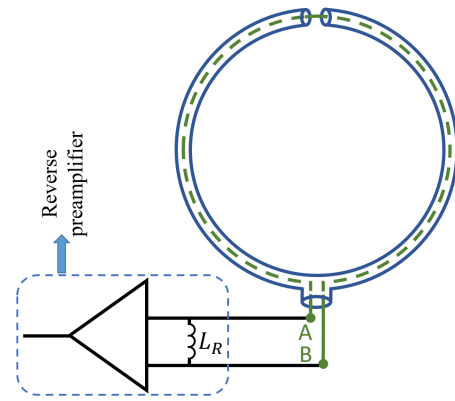

Fig. 1. Schematics of the HIC introduced in work [18] as an Rx antenna. With another matching circuit, this HIC can operate as a Tx antenna [20].

using it. This model has shown excellent agreement with full-wave simulations. Due to its simplicity, we consider it a useful design tool for prospective multiband HICs operating at frequencies up to microwaves.

II. Theory and Method

The generic HIC first suggested in paper [18] was an Rx antenna. It was made of a coaxial cable with a gap in the shield, as shown in Fig. 1. The receiver was connected to the antenna gap through a hole in the cable shield located at the counter-side of the gap. The induced electromotive force (IEMF) occurs on the shield exterior in this Rx antenna, and the gap in the shield allows the current to flow from the outer surface of the shield to its inner surface. The transformation of the receiver impedance through the coaxial cable dictates the input impedance seen by the IEMF which is very high at the resonance. In other words, in the presence of another Rx HIC, the self-impedance of the first receiver is much higher than the mutual impedance of the self-decoupled receiver.

Mollaei et al. [20] consider another matching circuit that transforms the Rx HIC from [18] into a Tx antenna suitable for MRI applications. That also found that introducing two additional symmetrically located gaps in the shield may transform the Rx HIC depicted in Fig. 1 into a transceiver HIC. Then, the same matching circuit may be used in both Rx and Tx regimes, preserving the self-decoupling property of this transceiver HIC.

In our next paper [21], the idea of putting more than one slit to obtain dual-band operation was discussed. Furthermore, in [23] we found a regime that turned out to be promising for WPT applications. In this regime, the current on the shield surface is low for an individual Tx HIC, and an HIC is used as an element of a Tx array with a coplanar arrangement. Meanwhile, in the presence of an Rx loop antenna at a reasonably small distance in front of the HIC, its radiating current drastically grows. This is because of the strong coupling between Rx and Tx, which results in a change in the inductance of the Tx that shifts its fundamental resonant frequency. Thus, the absolute value of the input impedance of the Tx dramatically drops, which allows the current to be fed in to instigate the radiation that is efficiently absorbed by the Rx [23]. This WPT system also allows variable positions of the Rx in front of the Tx array [23]. Practically, it is a WPT
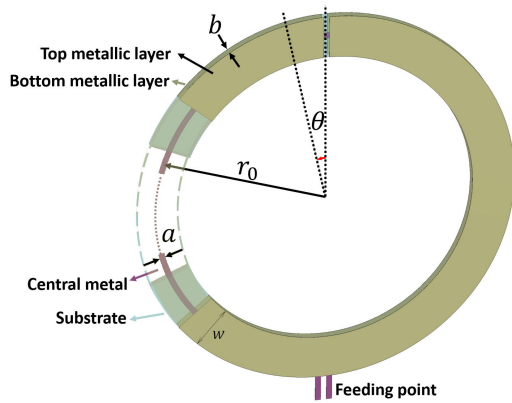
Fig. 2. Sketch of a single-band Tx HIC based on a stripline with a narrow slit at the polar angle θ (the same slit is made in both top and bottom metal strips). In the case of $\theta = 0$, the structure is symmetric with respect to the position of the slit. A part of the HIC is presented transparently to better show its interior. Note that here both the central metal and the substrate are continuous beneath the shield. The antenna feed is a narrow split in the central strip (not shown).

system with an automatic tracker of the presence and position of Rx.

In the current work, we apply the same general principle to a WPT system where the cable-based HIC is replaced by a stripline-based HIC whose single-band version is depicted in Fig. 2. The left part of this coil is presented partially transparent to show the interior of the stripline. The central metal strip of width a surrounded by the substrate material is sandwiched between two relatively wide strips of width w. Here, except at the feeding point, the central metal is continuous. This structure allows us to conveniently position slits at the central strip in addition to features discussed in Section I.

A. Tx Antennas

The central wire and the inner side of the shield form a transmission line (TL), whereas the outer side serves as a circular loop antenna. The impedance of the antenna consists of an inductance and a resistance, corresponding to the shield self-inductance and radiation resistance, respectively. The ohmic loss in this simplistic model was neglected. The input impedance, seen at the port, results from the transition of the outer shield impedance to the feeding point through the TL. The fundamental resonance of this antenna is that of a parallel circuit.

A straightforward way to design a Tx antenna is to perform extensive full-wave simulations with a wide range of all possible postures comprising various locations of the slits and dimensions of the antenna (the loop radius r_0, the widths w and a of the strips, the diameter of the dielectric disks on which the strips are printed, their thickness and their permittivity, and the permittivity of the substrate). In this way, one may optimize the antenna parameters for the desired operation frequency, however, this approach is extremely time-consuming and does not grant good insights into the antenna operation. Therefore, in Section III, we present a comprehensive circuit model of the HIC that allows us to calculate the antenna parameters rapidly and analytically. The circuit model covers the case of multiple slits in all three metal strips.

B. Decoupling of Transmitters

For WPT as well as for MRI applications, decoupling in arrays of Txs plays a critical role. In particular, it means that in the absence of the Rx, the coupling coefficient between the Txs should be practically nullified. Indeed, HICs utilized as Rx antennas are self-decoupled, but HICs used as Tx antennas need to be decoupled via optimization of mutual location, which is not so easy if the WPT system is compact. In the case of freely positioning Rxs, coupling between Txs partially occurs via Rxs and perfect decoupling is not possible. However, this coupling is not critical, and two Txs are decoupled in the absence of the Rx. If decoupling is required only in a low-frequency band (of the order of 150 MHz and lower), it would be simple because, in this frequency range, the current distribution on the external sides of the outer strips is uniform, similar to the outer surface of the shield in the case of the cable-based HIC [20], [21]. Then, the coupling of adjacent Txs is purely inductive and can be nullified by their partial overlapping. This overlapping is a well-known method of decoupling simple loop antennas operating at low frequencies. For HICs, the efficiency of this approach was confirmed in our works [20], [23]. However, we need decoupling also in the second band (540 MHz) where we observe a noticeable impact of the electric dipole mode in the simulated current profile not only in the interior, but also on the exterior of the effective shield.

For clarification, to decouple two circular antennas in which the current profile is uniform and the relative rotation of the circles does not affect the coupling, one overlaps two circles in an optimal way [18], [19], [20]. However, at higher frequencies, the current profile on the shield exterior becomes nonuniform. Both simulations and measurements confirm that in the second band, the Tx near-field pattern becomes similar to that of a Huygens element [21]—balanced electric and magnetic modes over the current profile. In this case, the radiation pattern of the antenna is a directive one with minimum radiation toward the feeding point and maximum radiation toward $\theta = 0$. As explained in [21], one efficient way to decouple two Huygens antennas is to overlap them upside-down with respect to each other (see, e.g., Fig. 9 in [21]). This upside-down overlapping grants maximal decoupling in both operation bands determined by two very distant parallel resonances. In the present work, we have adopted the same approach for two Txs based on the stripline operating at 131 and 540 MHz. In this work, we obtain a parallel resonance operation of an HIC at 540 MHz in a different way compared to [21], namely, we utilize the electric dipole resonance of the internal loop.

C. Rx Antennas

Rx antennas can be conventional one-turn loop antennas that experience series resonances at the operation frequencies of the Tx. One Rx is dedicated to Rx the power at 131 MHz and another one at 540 MHz, but they both need to have the loop radius around r_0 to be sufficiently coupled with the Txs for different positions of the Rx [23]. Since both Rx loops have the same self-inductance L_l, different lumped capacitors are
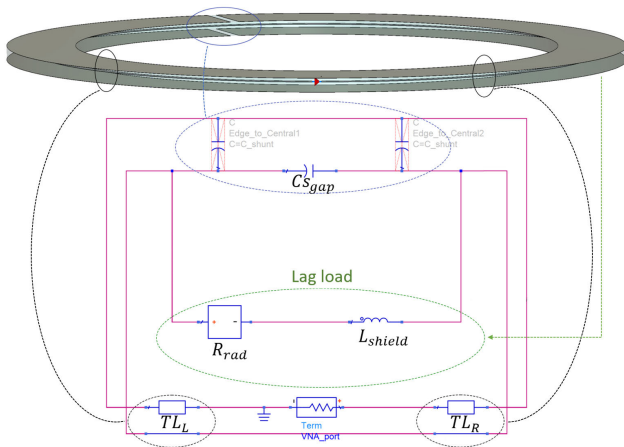
Fig. 3. Circuit model corresponding to the single-slit HIC (one slit in both outer strips). The red arrow in the inset shows the antenna input location (that is connected to the vector network analyzer).

used for tuning their resonances. Two values of capacitance C_l were found from full-wave simulations because the quasistatic formula for the resonance frequency ($\omega_0 = 1/\sqrt{L_l C_l}$) is not accurate enough even at 131 MHz (and is qualitatively inadequate at 540 MHz).

III. CIRCUIT MODEL OF THE Tx ANTENNA

First, we explain the developed circuit model for the simplest stripline-based HIC having one slit in the top and bottom metal strips, and then we extend this model to the case of two slits in both top and bottom strips. Finally, we present the most general model when there are two slits in the top and bottom strips and also one slit in the central strip (besides the antenna input gap).

A. Single-Slit HICs

For generality, assume the split to be located at an arbitrary angle, not necessary at $\theta = 0$ as shown in Fig. 2. Let us describe the impedance connected to this slit via each of the two parts of the HIC, not necessarily identical. Then, there are two nonidentical TLs (striplines) between the feeding point (antenna input) and the slit. The slit creates three effective capacitors: two equivalent capacitors formed by charges accumulated at the edge of the slit and the charges induced in the central metal strip, and one capacitor between the two edges. The two edge-to-central strip effective capacitors have shunt connections with the edge-to-edge capacitance. The lag load (consisting of the inductance and radiation resistance of the outer surfaces of the top and bottom strips) is connected in parallel to this total slit capacitance. Fig. 3 illustrates this circuit model. In this figure, we introduced links showing the correspondence of each element of the effective circuit to the relevant parts of the HIC shown in the top inset. In the notations of the circuit model, TL_L and TL_R stand for TLs connecting the feeding point to the slit in the clockwise and counterclockwise directions, respectively. Cs_{gap} stands for the total slit (gap) capacitance, R_{rad} stands for the radiation resistance of the antenna (due to its outer strips), and L_{shield} stands for the inductance of the outer strips.

When the slit is located at the angle θ, the lengths l_R and l_L of TL_R and TL_L, respectively, are as follows:

$$l_R = \left(1 + \frac{\theta}{180}\right) \times \pi r_0, \quad l_L = \left(1 - \frac{\theta}{180}\right) \times \pi r_0. \quad (1)$$

The input impedance of both microstrip TLs is calculated in the usual way via these lengths, whereas their characteristic impedance is the same and can be found, for example, in [24]

$$Z_0 = \frac{30\pi}{\sqrt{\epsilon_r}} \frac{b}{a_e + 0.441b} \quad (\Omega) \quad (2)$$

where ϵ_r is the relative permittivity of two dielectric spacers, b is their thickness, and a_e is the effective width of the central metal strip which is equal to the physical width a when $a/b > 0.35$. For calculating the radiation resistance, we study the current profile on the outer surface of the outer split strip treating it as a loaded wire loop of radius r_0. This study allows us to share the magnetic dipole (uniform) current mode and the electric dipole mode having zeros at the opposite points of the effective loop. The nonuniformity of the current across the strip width is not important because $r_0 \gg w$ and the approximation of a thin effective wire loop turns out to be adequate. If the electric dipole mode on the outer sides of the wide strips is sufficiently small, the radiation resistance is calculated as (see, e.g., in [25])

$$R_{\text{rad}} = 320\pi^4 \frac{S^2}{\lambda^4}. \quad (3)$$

Here, $S = \pi r_0^2$ is the loop area and λ stands for the wavelength in free space. In (3), we take into account that two outer strips are fully analogous to two halves of the cable shield. Really, the used stripline can be treated as a modified cable whose shield is cut in the meridian plane (this cut crosses the current lines) before unfolding its two halves. Therefore, the operation of the cable shield is mimicked namely by the pair of wide strips, and the loop antenna is effectively a single-turn one. In fact, in the whole range of relevant frequencies, the electric dipole mode is noticeable in the current flowing on the internal sides of the wide strips and on the narrow strip. However, these currents exactly cancel out, and the radiation is solely produced by the current flowing on the external side of the effective shield (the two outer strips). In this current, the electric dipole mode becomes significant only above 600–650 MHz.

The total inductance of the effective shield connected to the gap in accordance with [25] is equal to

$$L_{\text{shield}} \approx \frac{4\mu_0 N^2 R_1 (\alpha + 1)}{ln^2 \alpha} [E(k_0) - 1] \quad (4)$$

where E is the elliptic integral of the second kind, $R_1 = r_0 - w/2$ is the disk inner radius, $\alpha = (r_0 + w/2)/(r_0 - w/2)$ is the ratio between the outer and inner radii of the disk, and k_0 is a constant defined by

$$k_0 = \frac{4\alpha}{(\alpha + 1)^2}. \quad (5)$$

Since there is no analytical model for Cs_{gap} in the available literature, this quasistatic parameter is calculated numerically. In principle, it can be done in the static limit for a straight
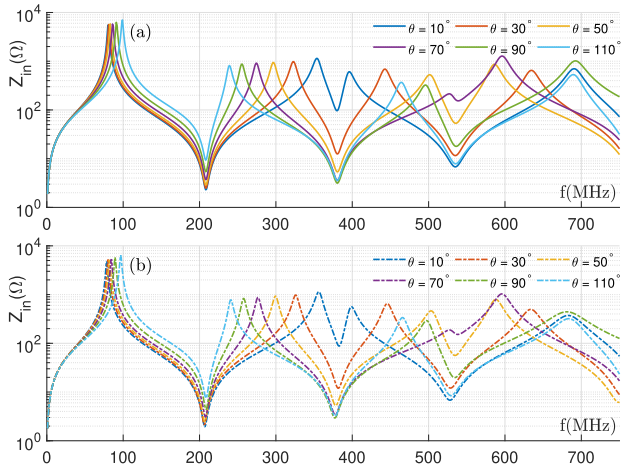
Fig. 4. Absolute value of the input impedance of the HIC with one asymmetrically located slit in the effective shield (outer strips). The angle of the slit runs over the following values: $\theta = 10°$, $30°$, $50°$, $70°$, $90°$, $110°$. (a) Circuit model. (b) Full-wave simulation.

stripline via a numerical solution of a boundary integral equation. However, for simplicity, we retrieved this value from full-wave simulations (CST studio). First, we simulate the input impedance of a symmetric single-slit HIC. Second, we fit it to the circuit model in ADS. When the value of Cs_{gap} is known, we can change the location angle θ of the slit for its asymmetric location and introduce other slits, if needed. Only Cs_{gap} is calculated numerically, whereas the other operating parameters of the antenna are analytically determined. In addition, after investigating the compatibility of the circuit model with the full-wave simulation for various cases, we found the shunt capacitors practically negligible. This is why we have hatched (opened) them in Fig. 3.

To verify the proposed circuit model, we compare the results obtained with the circuit model and with the use of CST Microwave Studio for an HIC with the following dimensions: $r_0 = 60$ mm, $a = 2$ mm, $w = 15$ mm, $b = 3$ mm, and the slit width 2 mm for different values of θ. The substrate permittivity is $\epsilon_r = 4.3$ (FR4 in the lossless approximation). In this case, the characteristic impedance of the TLs turns out to be equal $Z_0 = 40.6$ Ω, the outer strip inductance is $L_{shield} = 188.2$ nH, and the radiation resistance $R_{rad} = 1.974 \times 10^{-33} \times f^4$ Ω (f stands for the frequency in Hz). The retrieved value for Cs_{gap} for $\theta = 0$ is equal to 1.60 pF. Varying θ, we calculated the input impedance of the coil for different locations of the slit. Fig. 4 shows the results for the absolute values of the input impedance versus frequency obtained for different θ. On the top plot, these frequency curves are obtained from the circuit models, and on the bottom one—by full-wave simulations. We see an excellent agreement between the circuit model and numerical simulations below 650 MHz, where the electric dipole current mode of the effective shield becomes important. Similarly good agreement was achieved for the input impedance phase. This comparison convincingly confirms not only the qualitative veracity of the proposed circuit model, but also its quantitative accuracy. The developed model is useful for engineering HICs because the calculation time by the ADS software (into which the circuit model was uploaded) is incomparably shorter than the time of the corresponding full-wave simulations, for example, in CST Studio.
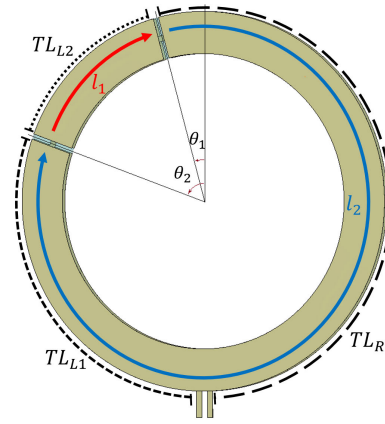

Fig. 5. Proposed HIC with two identical but arbitrarily located slits in the outer strips. L_1 and L_2 represent different parts of the outer strips engendering the lag loads. TL_R, TL_{L1}, and TL_{L2} represent TLs created by the central metal and inner surface of the outer strips.
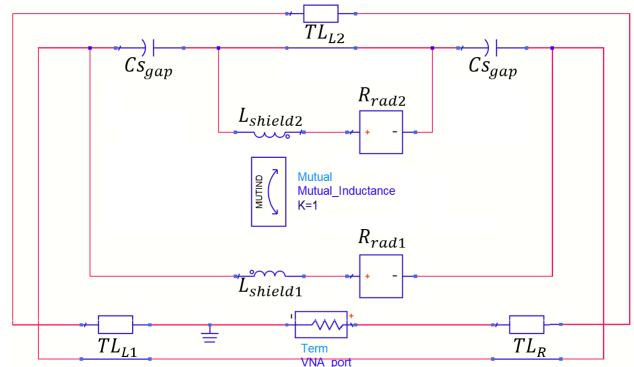

Fig. 6. Circuit model corresponding to dual-slit HICs. The MUTIND module represents the integral coupling between $L_{shield1}$ and $L_{shield2}$.

B. Two Slits in the Effective Shield

When a second slit is added to the effective shield, the circuit model needs to be modified. Adding a slit means adding an effective capacitor and the mutual inductance (between the inductors corresponding to divided effective shield parts by the slit) to the circuit model. This additional capacitor splits the lag load into two parts and the same split holds for one of the TLs. Fig. 5 shows an HIC with two slits in the effective shield. Here, the slit at θ_1 is the same as above, and the slit at θ_2 is added.

The circuit model for an HIC with two slits is shown in Fig. 6. In this case, there are three TLs in the circuit model: TL_R from the feeding point to the slit θ_1, TL_{L1} from the feeding point to the slit θ_2, and TL_{L2} from the slit θ_2 to the slit θ_1. Indeed, each of the two slits acts as a capacitor inserted in series between two TLs. When the second slit is added, the lag load described above (including the inductance and the radiation resistance of the external side of the effective shield) is divided into two parts. One lag load corresponds to the shield exterior from θ_1 to θ_2, and it is shown as l_1 in Fig. 6. Another lag load corresponds to that from θ_2 to θ_1 l_2. It is shown as l_2 in Fig. 6. The radiation resistance of the shield is distributed uniformly per unit length of the loop, and partial radiation resistances corresponding to l_1 and l_2 are as follows:

$$R_{rad1} = \frac{l_1}{l_1 + l_2} R_{rad}, \quad R_{rad2} = \frac{l_2}{l_1 + l_2} R_{rad} \quad (6)$$

where $R_{\rm rad}$ is given by 3. In accordance to the quasistatic theory of multisplit loops [26], [27], partial inductances corresponding to l_1 and l_2 are as follows:

$$L_{\rm shield1} = \frac{l_1^2}{(l_1 + l_2)^2} L_{\rm shield}, \quad L_{\rm shield2} = \frac{l_2^2}{(l_1 + l_2)^2} L_{\rm shield} \quad (7)$$

where $L_{\rm shield}$ is given by (4). Two inductances $L_{\rm shield1}$ and $L_{\rm shield2}$ are coupled to each other. Mutual coupling is modeled by two mutual inductances [27]

$$L_{\rm m} = \frac{l_1 l_2}{(l_1 + l_2)^2} L_{\rm shield}. \quad (8)$$

This formula corresponds to the parallel connection of $L_{\rm m}$ and $L_{\rm shield1,2}$. In a scheme with a series connection of the self- and mutual inductances [27], the mutual inductance is negative. In both cases, the mutual coupling decreases the inductances $L_{\rm shield1}$ and $L_{\rm shield2}$, as it must be for coplanar conductors [26], [27]. The identity

$$\frac{1}{L_{\rm shield}} = \frac{1}{L_{\rm shield1}} + \frac{1}{L_{\rm shield2}} + \frac{2}{L_{\rm m}} \quad (9)$$

expresses the fact that two inductances $L_{\rm shield1}$ and $L_{\rm shield2}$ and two mutual inductances $L_{\rm m}$ form a complete loop with the inductance $L_{\rm shield}$ [26].

The total inductance of the parallel connection of $L_{\rm shield1,2}$ and $L_{\rm m}$ can be denoted as $L'_{\rm shield1,2}$. Lag load 1 consisting of $R_{\rm rad1}$ and $L'_{\rm shield1}$ is connected in parallel to TL_{L2}, lag load 2 ($R_{\rm rad2}$ and $L'_{\rm shield2}$) is in a parallel connection to the series circuit of three elements $TL_{L1} + source + TL_R$, where $source$ denotes the antenna gap.

So, we can describe the addition of a slit to the effective shield in the following modifications of our circuit model as follows.

1) Inserting an effective capacitor into one of the TLs.
2) Splitting the corresponding TL into two TLs connected by this capacitor.
3) Splitting the lag load corresponding to the effective shield exterior into two loads. Radiation resistances of the new lag loads are proportional to the lengths of these parts. The inductance of the lag loads is proportional to the square power of these lengths.

To verify the proposed circuit model, we compare the results of the ADS circuit model and that of CST Microwave Studio for an HIC with two slits. The geometry and material properties of this coil are the same as for the HIC from Section III-A, except for the location of the slits. In this example, $\theta_1 = -30°$, whereas the angle of the second slit varies in the range [10° : 20° : 110°]. From Section III-A, we know that for this geometry $C_s = 1.60$ pF, $L_{\rm shield} = 188.2$ nH, and $R_{\rm rad} = 1.974 \times 10^{-33} \times f^4 \Omega$. Then, using (6) and (7), we deduce $R_{\rm rad1}$, $R_{\rm rad2}$, $L_{\rm shield1}$, and $L_{\rm shield2}$. Changing the location of the second slit, we change l_1 and l_2, that is, vary the lengths of the two TLs, their effective radiation resistances $R_{\rm rad1}$ and $R_{\rm rad2}$, and their effective inductances $L'_{\rm shield1}$ and $L'_{\rm shield2}$. Fig. 7 depicts the results obtained by the ADS circuit model and CST Studio, which show an excellent agreement between them until approximately 600 MHz. Notice that in the case of two slits in the effective shield, the electric
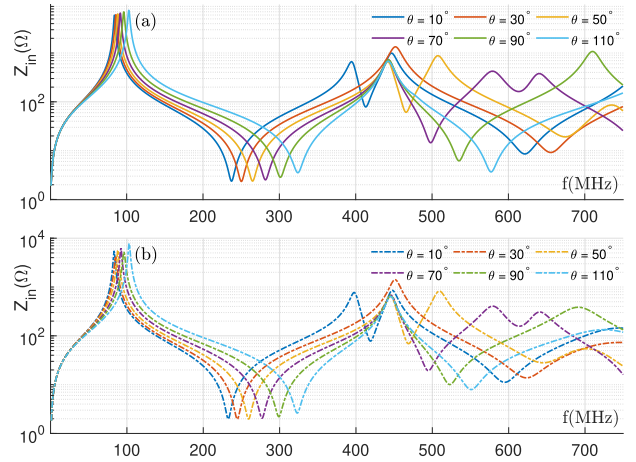

Fig. 7. Absolute value of the input impedance of the HIC with two slits in the effective shield. One slit is fixed at $\theta_1 = -30°$ and the other slit location angle runs over the following values: $\theta_2 = 10°, 30°, 50°, 70°, 90°, 110°$. (a) Circuit model. (b) Full-wave simulation.

dipole mode in the external current becomes noticeable already starting from 400 MHz. However, its negligence brings a rather small error into the absolute values of the input impedance at frequencies below 600 MHz.

C. Two Slits in the Effective Shield and One Slit in the Central Strip

When a slit is added to the central (narrow) strip, a capacitance is created between the edges of the slit and two capacitances connected in series arise between the slit edge and the effective shield. Indeed, the corresponding TL is also split into two parts. However, unlike a slit in the effective shield, the slit in the central strip does not change the lag load because it does not reshape the shield. Also, the capacitance due to this slit is inserted into another effective wire of the model two-wire TL, with respect to the slit in the shield. Since in Fig. 5, the slit in the shield is referred to as the "grounded" wire of the TL, in the present case, the internal slit capacitance C_i (keeping the notation C_s for the slits in the effective shield) is inserted into the "biased" wire. The circuit model is presented in Fig. 8. The antenna illustrated by this figure differs from the coil depicted in Fig. 5 by one slit in the central strip located in the middle between the antenna gap and the position θ_2. This slit divides TL_{L1} into two TLs, TL_{L11} and TL_{L12}, which are connected by C_i. The value of this C_i needs to be calculated numerically, similar to what we did for C_s. Full-wave simulations by CST Studio verified the accuracy of this circuit model, as well. For HICs with more slits in the outer and/or central strips, the same approach can be used in an extended form.

IV. DESIGN, SIMULATIONS, AND MEASUREMENTS OF THE WPT SYSTEM

Based on the described circuit model, we designed a dual-band stripline-based Tx HIC. Furthermore, a WPT system based on two such Txs and two conventional Rxs (one for each band) has been designed, fabricated, and studied. Simulations were made with the use of CST Microwave Studio. Experimental verification was done via an S-parameters measurement with further retrieval of all relevant parameters.
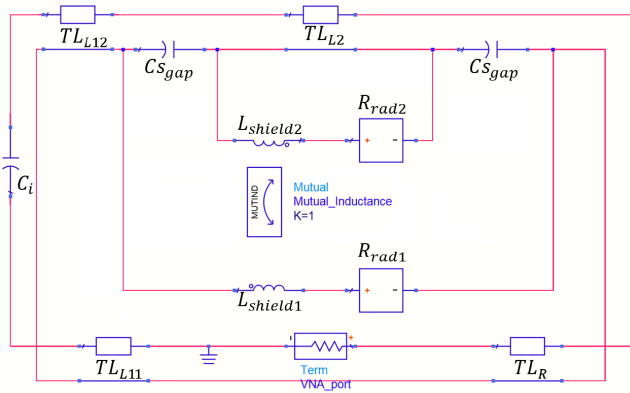
Fig. 8. Circuit model corresponding to HICs with two slits in the outer strips and one slit in the central metal strip between the feeding point $\theta = \pi$ and θ_2.
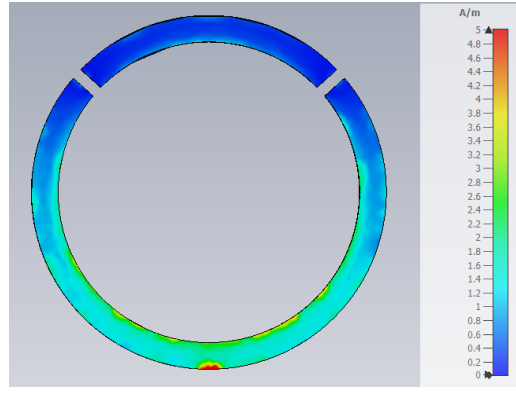
In the experiment, we used the Rohde Schwarz ZND Vector Network Analyzer. To analyze the performance of the system, we first tested each Tx and Rx in both operation bands. Then, we numerically and experimentally studied the coupling of the two Txs and found an identified regime of maximal decoupling in both bands. Finally, we placed the Rx on top of the array of Txs and varied the Rx location in front of it. Note that the decoupling of Txs in both bands was achieved simultaneously.

A. Tx Antennas

The two tested operation bands are centered at 131 and 540 MHz, respectively. In accordance with [23], the optimal performance of a Tx HIC in WPT applications occurs at a frequency slightly higher than its resonant frequency. Therefore, the Tx is designed so that to resonate at 113 and 506 MHz. To estimate the impact of the dielectric substrate, we designed the Tx based on FR4 and Rogers RT5880 substrates, although the experimental verification has been done only for the FR4 substrate. Therefore, the analysis for the FR4 substrate is reported below completely, and for Rogers RT5880, we present only simulated efficiency at the two operating frequencies.

The optimization of the Txs follows Section III. First, we define the geometrical constraints and material properties of the coil and then apply our circuit model in which we vary the locations of two symmetric gaps to obtain the resonances at the required frequencies. The dimensions of the coil designed based on FR4 (sheets having a thickness equal to 1.5 mm and a relative permittivity of 4.3) are $r_0 = 43$ mm, $w = 7$ mm, $a = 0.4$ mm, $b = 3$ mm, and the metal thickness $t = 35$ μm. Next, we perform the fine optimization using ADS and CST Microwave Studio. Finally, two splits are located symmetrically at $\theta_1 = 48°$ and $\theta_2 = -48°$, as shown in Fig. 2. In these simulations, we take into account that the connectors of the antenna gap (as well as the coil strips) are printed on an FR4 substrate. These connectors grant a small additional capacitance shunting the feeding point (that leads to nearly 5% disagreement with the circuit model).

The symmetric location of two gaps in the effective shield (no gap in the central strip) allows a parallel resonance above 500 MHz for our HIC. Unlike the cable-based HIC with two asymmetric gaps on the shield [21], the stripline-based HIC with symmetric gaps does not offer purely balanced electric and magnetic dipole modes in the current distribution at the second resonance. In addition to these modes, the current
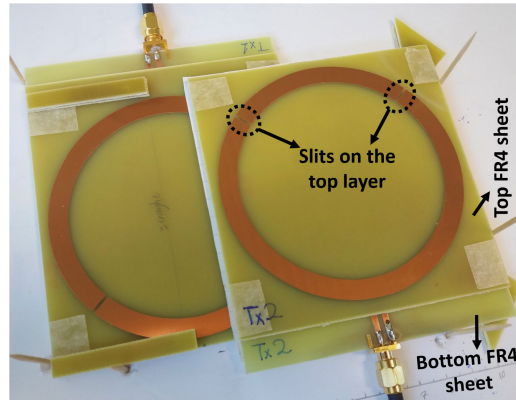

Fig. 9. Current distribution over the outer surface of the effective shield at the second resonance.

Fig. 10. Fabricated Tx1 and Tx2 printed on FR4 sheets. The connectors are attached to the central metal strip. Two Txs are overlapped upside-down by 30% to be decoupled at both bands simultaneously.

profile contains a hybrid mode. However, approximately the balance between the electric and magnetic dipole modes is achieved, and the radiation pattern of our HIC is close to that of the Huygens antenna. Fig. 9 shows the current distribution over the outer surface of the effective shield at the second resonance, being similar to the Huygens profile discussed in [20]. As we explained in Section II-B, this Huygens-type pattern ensures the decoupling of two adjacent HICs at 540 MHz.

Two prototypes of the Tx have been fabricated and their input impedances (practically identical) measured. The top strip was printed on one side of an FR4 sheet, and the central and bottom strips were printed on the two sides of another FR4 sheet. These two disk-wise sheets were glued, and the optimal overlapping to the HICs needed for decoupling at 131 MHz was ensured.

So, two dual-band Txs based on HICs can be decoupled in both bands simultaneously using partial overlapping and locating the feeding points upside-down, as it is shown in Fig. 10. In the numerical study, two HICs are optimally overlapped by 26 mm. If we use in simulations ideal matching circuits connected to the antenna gap, we obtain $S_{11} \approx -50$ dB at both operational frequencies. Despite this almost perfect matching, that implies maximal excitation of the Tx antenna, the coupling coefficients of two antennas are as small as $S_{21} = S_{12} = -25$ dB at 131 MHz and -20 dB at 540 MHz. So, on the level of numerical simulations, our Tx array is optimized.
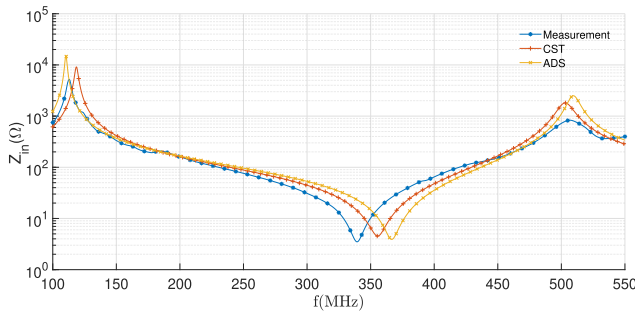
Fig. 11. Absolute value of the input impedance of Tx obtained by the circuit model in ADS (dotted), full-wave simulations in CST (stars), and measurements (squares).

The experiment has shown another optimal overlapping—32 mm. The difference is probably related to the action of the dielectric parts of the system (the glue, the exact shape of the dielectric disks, etc.) which cannot be exactly taken into account in simulations. To avoid the fabrication of dual-band matching circuits, S-parameters of the Txs were measured in the mismatched regime and exported to ADS software. Two virtual matching circuits were added to the coils and the return loss of -40 dB was achieved in both bands. Coupling between Txs in this virtually matched regime is much higher than the directly measured S_{12}. Namely, we got $S_{12} = -11$ dB at 131 MHz and $S_{12} = -9.4$ dB at 540 MHz. In the literature, this level of coupling is considered acceptable (see, e.g., in [23]).

Fig. 11 shows the measured absolute value of the input impedance in comparison with calculations. We observe a good agreement between numerical and experimental results. The reasons for small disagreements are discussed above.

If the same strips are printed on similar disks of Rogers RT5880, the same resonance and operational frequencies can be obtained, whereas this low-loss substrate (the loss tangent 0.00122 against that equal to 0.02 for FR4) would grant higher values of the input impedance at the operating frequencies. This would promise higher power transfer efficiencies in both bands.

B. Rx Antennas

As it was explained in Section III, two conventional loop coils with the same size as Txs were designed. These simple loops were also printed on FR4 substrates. Three lumped capacitors were added to each of the two loops to grant a resonance at the required frequency. Capacitors with capacitance $C = 19$ pF were inserted into Rx1 and granted the resonance at 131 MHz. Capacitance $C = 1$ pF inserted into Rx2 granted a resonance at 540 MHz. Fig. 12 shows the complete experimental setup in which Rx2 with its three capacitors is seen.

C. System Performance

To analyze the performance of the proposed WPT system, we followed our previous work [23]. First, we place the Rx at different positions and see how the input impedance of each Tx drops. Second, we analyze the stability of the received power versus the position of the Rx. Third, we analyze the efficiency of the whole system in both bands versus the Rx positions. The distance between the surface of the Tx array
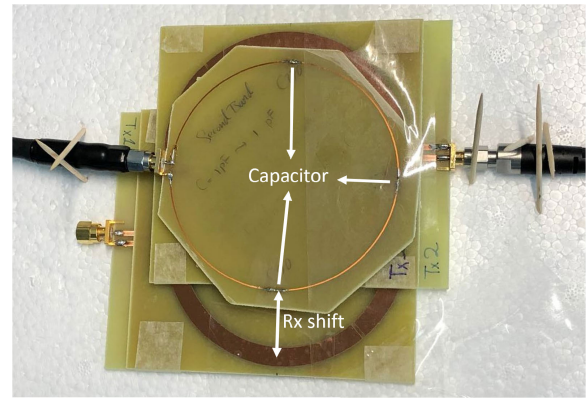

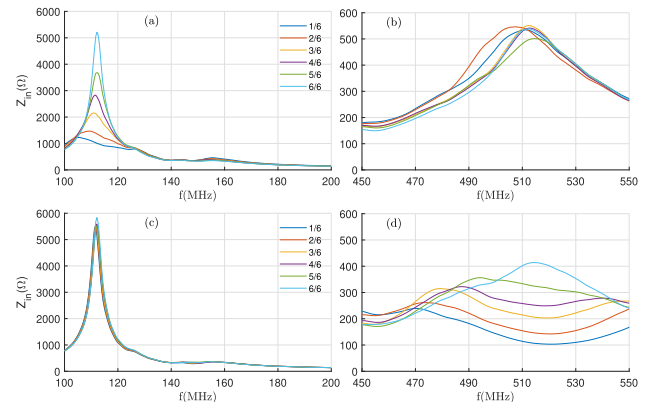Fig. 12. Tested WPT system with two Txs and one Rx antenna (Rx2).

Fig. 13. Decrease of the Tx1 input impedance versus frequency for six different locations of Rx1 and Rx2. (a) and (b) Impact of Rx1 for the first and second bands, respectively. (c) and (d) Impact of Rx2 for the first and second bands, respectively. In the legend, the shift of Rxs is normalized to the distance between the centers of two Txs, so 6/6 means the Rx is exactly over Tx2.

and that of the Rxs is equal to 14 mm. This gap was filled with foam. Fig. 13 shows the absolute value of the input impedance of Tx1 with respect to the position of Rx1 and Rx2. As expected, in the presence of Rx, the input impedance of Txs at the corresponding operational frequency strongly drops, which is the prerequisite of effective WPT. The magnitude of this decrease depends on the location of the Rx. When the Rx is located exactly in front of Tx1, the decrease is maximal. Indeed, each of the two Rxs affects Z_{in} of the Tx namely in its operational band, having no impact on the input impedance of the Tx in the other band. Fig. 13(a) and (b) illustrates the impact of Rx1 for the first band, and Fig. 13(c) and (d) does the same for the second band. These results confirm the concept of the proposed WPT system.

Fig. 14(a) and (b) shows the power accepted by both Txs and the power received by Rxs with respect to the positions of Rx1 or Rx2. Both powers are normalized to the maximal total power $P_{Txs} = P_{Tx1} + P_{Tx2}$ accepted by the Tx array from the source (to which they are both connected through a power divider) in the corresponding band. As expected, the received power by Rx1 is position-stable in the first band and the power accepted by each of the two Txs drastically increases if Rx1 is located in front of a Tx. In the second band, due to a more directional pattern of Txs, the received power is not similarly stable. In this band, Rx2 affects the coupling between two Txs. However, the distance of 14 mm between the plane of the Rx and the surface of the Tx array allows us to keep this parasitic
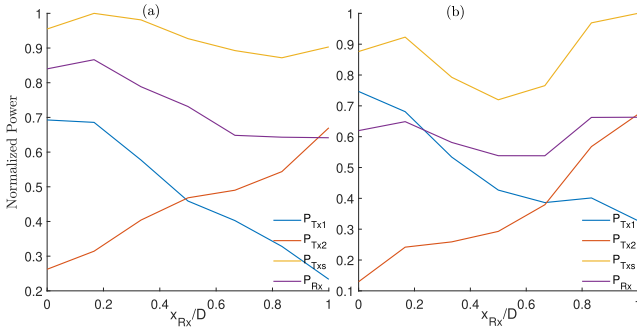
Fig. 14. Normalized power delivered to Tx1 and Tx2 and normalized power received by the receiver versus the position of the Rx antenna. (a) First band (Rx1). (b) Second band (Rx2).

Fig. 15. Efficiency of the proposed system (experimental and numerical results) at frequencies f_1 (denoted as η_1) and f_2 (η_2) versus the relative position of the corresponding Rx. Curve for η_1 marked "Mea + C_{Rx1}" corresponds to the theoretically added matching circuit with the optimal shunt capacitor.

effect at an acceptable level. Fig. 14(b) shows that the power received by Rx2 is stable enough, though not perfectly.

Now let us discuss the efficiency of the system. The power transfer efficiency η is defined as the ratio between the received power by Rx (Rx1 at the first band and Rx2 at the second band) to the power $P_{\text{Txs}} = P_{\text{Tx1}} + P_{\text{Tx2}}$ accepted by two Txs from the source. The efficiency can be calculated directly from the accepted and received powers depicted in Fig. 14), or it can be calculated via the S-parameters. The result is the same, but it is instructive to express η via the S-parameters analytically. We have

$$P_{\text{Tx1}} = 1 - |S_{11} + S_{12}|^2, \quad P_{\text{Tx2}} = 1 - |S_{21} + S_{22}|^2 \quad (10)$$

where $S_{12} = S_{21}$ due to reciprocity, and the received power is calculated as follows:

$$P_{\text{Rx}} = |S_{31} + S_{32}|^2. \quad (11)$$

The efficiency can be then presented as

$$\eta = \frac{P_{\text{Rx}}}{P_{\text{Tx1}} + P_{\text{Tx2}}} = \frac{|S_{31} + S_{32}|^2}{2 - |S_{11} + S_{12}|^2 - |S_{22} + S_{12}|^2}. \quad (12)$$

Fig. 15 shows the efficiency of the system in the first and second bands obtained from simulations and measurements in accordance to (12). We have already mentioned with reference to [23] that the maximal efficiency occurs at a frequency slightly higher than the parallel resonance frequency of an individual Tx. An additional study has shown that the maximal efficiency of the WPT system occurs at the parallel resonance frequency of the input impedance of Tx1 in the presence of Tx2 (or vice versa) when it is located optimally, that is, when two Txs are maximally decoupled. The self-impedance of both Txs experiences individual resonances at 113 and 506 MHz, respectively, and the operational frequencies 131 and 540 MHz correspond namely to the resonances shifted due to the coupling of antennas.

In Fig. 15, besides the directly calculated η, we also present the efficiency curve calculated for the first band when the experimental data is exported to ADS and Rx1 is shunted with a 15-pF capacitor. This technique shows that the optimal matching can increase the efficiency at least in the first band by nearly 5%. Finally, we obtain the experimental efficiency of the system for all adopted positions of the Rx not less than 85% and 73% for the first and second bands, respectively.

Still, the efficiency of this system in the first band is smaller by nearly 5% when compared to that obtained in [23] for a
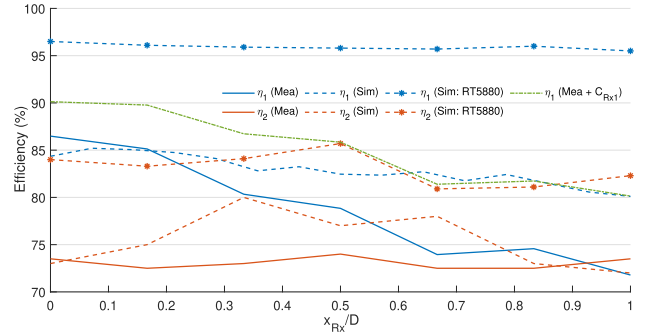
TABLE I
COMPARISON OF STRIPLINE AND COAXIAL [23] HICs

Features	Coaxial [24]	Stripline (This work)
Efficiency	96%, –	96%, 84% (RT5880 substrate)
Multibandness	No	Yes
Structural manipulation	Hard	Easy
Manufacturing accuracy	Moderate	Very high
Decoupling	High	High

single-band WPT system with the same distance between the Rx and Tx arrays. This worsening is mainly due to the use of an FR4 substrate, whereas in [23], the antenna was based on a commercial low-loss coaxial cable, practically not sensitive to the Teflon substrate.

Numerical simulations show that when FR4 is replaced by Rogers RT5880, the efficiency increases drastically and exceeds both theoretical and experimental results obtained for cable-based HICs [23]. As we can see in Fig. 15, the position-averaged efficiency of the system based on RT5880 will be equal to 96% and 84% at the first and second bands, respectively. Deviations from the position-averaged value of the efficiency are very small, especially in the first band.

V. CONCLUSION

A dual-band self-activating HIC based on striplines has been suggested and studied for WPT applications as an element of the Tx antenna array. Compared to previously reported HICs for WPT applications, the proposed design has the advantage of dual-band operation. Moreover, the replacement of a cable with a stripline allows us to overcome the restrictions to the minimal radius of the coil and locate the second frequency band above 500 MHz. A WPT system constituted by two Txs and two Rxs (one for each operational band) has been designed and fabricated. Numerical and experimental results show stable highly efficient performance in both the first and second frequency bands. It was numerically shown that the use of commercially available low-loss substrates will further improve the efficiency. In this work, a versatile circuit model was developed, which is suitable not only for the suggested HICs but also for prospective HICs with more slits in the central and/or external strips. Table I compares the major features of the coaxial [23] and stripline arrangement.

ACKNOWLEDGMENT

REFERENCES

[1] X. Dai, X. Li, Y. Li, and A. P. Hu, "Maximum efficiency tracking for wireless power transfer systems with dynamic coupling coefficient estimation," *IEEE Trans. Power Electron.*, vol. 33, no. 6, pp. 5005–5015, Jun. 2018.

[2] X. Liu and S. Y. Hui, "Optimal design of a hybrid winding structure for planar contactless battery charging platform," *IEEE Trans. Power Electron.*, vol. 23, no. 1, pp. 455–463, Jan. 2008.

[3] U.-M. Jow and M. Ghovanloo, "Geometrical design of a scalable overlapping planar spiral coil array to generate a homogeneous magnetic field," *IEEE Trans. Magn.*, vol. 49, no. 6, pp. 2933–2945, Jun. 2013.

[4] W. X. Zhong, X. Liu, and S. Y. R. Hui, "A novel single-layer winding array and receiver coil structure for contactless battery charging systems with free-positioning and localized charging features," *IEEE Trans. Ind. Electron.*, vol. 58, no. 9, pp. 4136–4144, Sep. 2011.

[5] C. C. Mi, G. Buja, S. Y. Choi, and C. T. Rim, "Modern advances in wireless power transfer systems for roadway powered electric vehicles," *IEEE Trans. Ind. Electron.*, vol. 63, no. 10, pp. 6533–6545, Oct. 2016.

[6] S. A. Mirbozorgi, H. Bahrami, M. Sawan, and B. Gosselin, "A smart multicoil inductively coupled array for wireless power transmission," *IEEE Trans. Ind. Electron.*, vol. 61, no. 11, pp. 6061–6070, Nov. 2014.

[7] S. A. Mirbozorgi, H. Bahrami, M. Sawan, and B. Gosselin, "A smart cage with uniform wireless power distribution in 3D for enabling long-term experiments with freely moving animals," *IEEE Trans. Biomed. Circuits Syst.*, vol. 10, no. 2, pp. 424–434, Apr. 2016.

[8] F. Jolani, Y.-Q. Yu, and Z. Chen, "A planar magnetically-coupled resonant wireless power transfer using array of resonators for efficiency enhancement," in *IEEE MTT-S Int. Microw. Symp. Dig.*, May 2015, pp. 1–4.

[9] J. W. Kim et al., "Wireless power transfer for free positioning using compact planar multiple self-resonators," in *IEEE MTT-S Int. Microw. Symp. Dig.*, Kyoto, Japan, May 2012, pp. 127–130.

[10] S. Y. Hui, "Planar wireless charging technology for portable electronic products and Qi," *Proc. IEEE*, vol. 101, no. 6, pp. 1290–1301, Jun. 2013.

[11] A. Pacini, A. Costanzo, S. Aldhaher, and P. D. Mitcheson, "Load- and position-independent moving MHz WPT system based on GaN-distributed current sources," *IEEE Trans. Microw. Theory Techn.*, vol. 65, no. 12, pp. 5367–5376, Dec. 2017.

[12] W. Kim and D. Ahn, "Efficient deactivation of unused LCC inverter for multiple transmitter wireless power transfer," *IET Power Electron.*, vol. 12, no. 1, pp. 72–82, Jan. 2019.

[13] V. Jiwariyavej, T. Imura, and Y. Hori, "Coupling coefficients estimation of wireless power transfer system via magnetic resonance coupling using information from either side of the system," *IEEE J. Emerg. Sel. Topics Power Electron.*, vol. 3, no. 1, pp. 191–200, Mar. 2015.

[14] X. Dang, P. Jayathurathnage, S. A. Tretyakov, and C. R. Simovski, "Self-tuning multi-transmitter wireless power transfer to freely positioned receivers," *IEEE Access*, vol. 8, pp. 119940–119950, 2020.

[15] J. M. Arteaga, S. Aldhaher, G. Kkelis, C. Kwan, D. C. Yates, and P. D. Mitcheson, "Dynamic capabilities of multi-MHz inductive power transfer systems demonstrated with batteryless drones," *IEEE Trans. Power Electron.*, vol. 34, no. 6, pp. 5093–5104, Jun. 2019.

[16] S. Malhotra, S. Verma, V. Bohara, and M. Hashmi, "Dual-band WPT system using semi-H DGS for biomedical applications," in *Proc. IEEE Asia–Pacific Microw. Conf. (APMC)*, Singapore, Dec. 2019, pp. 720–722.

[17] A. Iqbal, P. R. Sura, M. Al-Hasan, I. B. Mabrouk, and T. A. Denidni, "Wireless power transfer system for deep-implanted biomedical devices," *Sci. Rep.*, vol. 12, no. 1, Aug. 2022, Art. no. 13689.

[18] B. Zhang, D. K. Sodickson, and M. A. Cloos, "A high-impedance detector-array glove for magnetic resonance imaging of the hand," *Nature Biomed. Eng.*, vol. 2, no. 8, pp. 570–577, May 2018.

[19] T. Ruytenberg, A. Webb, and I. Zivkovic, "Shielded-coaxial-cable coils as receive and transceive array elements for 7T human MRI," *Magn. Reson. Med.*, vol. 83, no. 3, pp. 1135–1146, Mar. 2020.

[20] M. S. M. Mollaei, C. C. Van Leeuwen, A. J. E. Raaijmakers, and C. R. Simovski, "Analysis of high impedance coils both in transmission and reception regimes," *IEEE Access*, vol. 8, pp. 129754–129762, 2020.

[21] M. S. M. Mollaei, A. S. M. Mollaei, and C. R. Simovski, "Dual-band transceiver high impedance coil array for ultrahigh field magnetic resonance imaging," *IEEE Trans. Antennas Propag.*, vol. 70, no. 2, pp. 1033–1044, Feb. 2022.

[22] L. Nohava et al., "Flexible multi-turn multi-gap coaxial RF coils: Design concept and implementation for magnetic resonance imaging at 3 and 7 Tesla," *IEEE Trans. Med. Imag.*, vol. 40, no. 4, pp. 1267–1278, Apr. 2021.

[23] M. S. M. Mollaei, P. Jayathurathnage, S. A. Tretyakov, and C. R. Simovski, "High-impedance wireless power transfer transmitter coils for freely positioning receivers," *IEEE Access*, vol. 9, pp. 42994–43000, 2021.

[24] D. M. Pozar, *Microwave Engineering*. Hoboken, NJ, USA: Wiley, 2011.

[25] C. A. Balanis, *Antenna Theory: Analysis and Design*. Hoboken, NJ, USA: Wiley, 2005.

[26] A. M. Siddiky, M. R. I. Faruque, M. T. Islam, and S. Abdullah, "A multi-split based square split ring resonator for multiband satellite applications with high effective medium ratio," *Results Phys.*, vol. 22, Mar. 2021, Art. no. 103865.

[27] A. E. Ruehli, "Inductance calculations in a complex integrated circuit environment," *IBM J. Res. Develop.*, vol. 16, no. 5, pp. 470–481, Sep. 1972.

Ali Jabbari was born in Tehran, Iran, in 1999. He received the B.Sc. degree in electrical engineering with a minor in physics from the Sharif University of Technology, Tehran, in 2022. He is currently pursuing the Ph.D. degree with the Department of Electrical and Computer Engineering, University of California, Los Angeles, CA, USA.

He attended a summer internship at Aalto University, Finland, for his Ph.D., B.Sc., in 2021. His current prime area of interest revolves around THz engineering, focusing on developing THz generators incorporating photomixers.
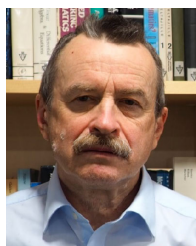
Constantin Simovski was born in Saint Petersburg, Russia, in December 1957. He received the Dipl.-Eng. degree (by Research) in radio engineering, the Ph.D. degree in electromagnetic theory, and the D.Sc. degree from Saint Petersburg State Polytechnic University (formerly Leningrad Polytechnic Institute (LPI), and State Technical University), Saint Petersburg, in 1980, 1986, and 2000, respectively. In 1986, he defended the Candidate of Science (Ph.D.) thesis (a study of the scattering of Earth waves in the mountains) at LPI. In 2000, he defended the D.Sc. thesis (a theory of 2-D and 3-D bianisotropic scattering arrays).

From 1980 to 1992, he was with the Soviet scientific and industrial firm "Impulse," Saint Petersburg. In 1992, he joined the Saint Petersburg University of Information Technologies, Mechanics and Optics, Saint Petersburg, as an Assistant Professor, where, from 1994 to 1995, he was an Assistant Professor, from 1995 to 2001, he was an Associate Professor, and, since 2001, he has been a Full Professor. Moreover, he has been a Full Professor at Aalto University, Espoo, Finland, since 2012. Since 1999, he has been involved in the theory and applications of 2-D and 3-D electromagnetic bandgap structures for microwave and ultrashortwave antennas. His current research interests include metamaterials for microwave and optical applications, including optics of metal nanoparticles.

Masoud Sharifian Mazraeh Mollaei was born in Tehran, Iran, in 1989. He received the M.Sc. degree in electrical engineering from the Iran University of Science and Technology (IUST), Tehran, in 2016, and the Ph.D. degree in electrical engineering from the Department of Electronics and Nanotechnology, Aalto University, Espoo, Finland, in 2021, where he has been developing theoretical and experimental techniques for ultrahigh-field magnetic resonance imaging.

Currently, he is a Senior Microwave Design Engineer at Harp Technologies Ltd. and a Post-Doctoral Researcher at the Department of Electrical Engineering and Automation, Aalto University. His current research interests include very low-field magnetic resonance imaging, ultrahigh-field magnetic resonance imaging, array antennas, antenna decoupling, metamaterials, photonics, and ferrite-based components.